ADVANCED FUNCTIONAL MATERIALS
www.afm-journal.de

Three-Dimensional Co_3O_4@MnO_2 Hierarchical Nanoneedle Arrays: Morphology Control and Electrochemical Energy Storage

*Dezhi Kong, Jingshan Luo, Yanlong Wang, Weina Ren, Ting Yu, Yongsong Luo, Yaping Yang, and Chuanwei Cheng**

In this paper, a highly ordered three-dimensional Co_3O_4@MnO_2 hierarchical porous nanoneedle array on nickel foam is fabricated by a facile, stepwise hydrothermal approach. The morphologies evolution of Co_3O_4 and Co_3O_4@MnO_2 nanostructures upon reaction times and growth temperature are investigated in detail. Moreover, the as-prepared Co_3O_4@MnO_2 hierarchical structures are investigated as anodes for both supercapacitors and Li-ion batteries. When used for supercapacitors, excellent electrochemical performances such as high specific capacitances of 932.8 F g^{-1} at a scan rate of 10 mV s^{-1} and 1693.2 F g^{-1} at a current density of 1 A g^{-1} as well as long-term cycling stability and high energy density (66.2 W h kg^{-1} at a power density of 0.25 kW kg^{-1}), which are better than that of the individual component of Co_3O_4 nanoneedles and MnO_2 nanosheets, are obtained. The Co_3O_4@MnO_2 NAs are also tested as anode material for LIBs for the first time, which presents an improved performance with high reversible capacity of 1060 mA h g^{-1} at a rate of 120 mA g^{-1}, good cycling stability, and rate capability.

1. Introduction

In recent years, electrochemical storage devices like supercapacitors and Li-ion batteries have attracted considerable attention due to their wide applications in portable electronics, hybrid electric vehicles and smart electricity grids that storing the intermittent energy sources such as solar, wind and tide.[1–4] Supercapacitors, also known as electrochemical capacitors (ECs), which can temporarily store a large amount of charge and then release it when needed by a non-faradaic electrical energy storage process, holds features in good pulse charging-discharging, long lifespan and high reliability and low maintenance cost.[5,6] They commonly store energy using either ion adsorption (electrochemical double layer capacitors, EDLCs) or fast surface redox reactions (pseudo-capacitors, PCs), basically, the former use carbon-active materials as electrodes and the latter use redox-active materials.[7] The other way of renewable energy storage, that is, LIBs, performing electrical work by Li^+ ion diffusion and faradaic oxidation/reduction of electrical reagents between the two electrodes usually offer large energy and power density in comparison to supercapacitors.[8,9] Currently, the research focus on electrochemical storage is the rational design of proper electrode with high capacity, large energy density and long cycling stability.[10–12]

Various materials, including carbonaceous materials,[13–15] transition metal oxides,[16–18] conducting polymers,[19–21] and hybrid composites,[22–24] have been widely studied as the electrode materials. Among them, nanostructured metal oxides, with high capacity and low cost are especially attractive for advanced electrodes. In particular, Co_3O_4 with theoretical specific capacitance (≈890 F g^{-1}) and MnO_2 (theoretical specific capacitance ≈1370 F g^{-1}) are widely investigated as supercapacitors due to their earth-abundance and environmental friendliness).[25,26] However, the Co_3O_4 suffers from poor capacity retention and rate capacity, and MnO_2 has bad conductivity (10^{-5}–10^{-6} S cm^{-1}), which greatly hinder their practical application with sole institute.[27–29] To address these problems, one way is design of MnO_2 based composites by using highly conductive materials like metal,[30] conducting polymer,[31,32] carbon nanotube[33,34] or graphene[35,36] as scaffolds for supporting MnO_2 nanostructured thin films to enhance the performance. Another strategy is integration of Co_3O_4@MnO_2 with a smart design to improve the performance due to the synergistic effects between the two components. For example, Liu et al.[37] reported Co_3O_4@MnO_2

D. Kong, W. Ren, Prof. Y. Yang, Prof. C. Cheng
Shanghai Key Laboratory of Special Artificial Microstructure Materials and Technology
School of Physics Science and Engineering
Tongji University
Shanghai 200092, P. R. China
E-mail: cwcheng@tongji.edu.cn
Dr. J. Luo, Y. Wang, Prof. T. Yu
Division of Physics and Applied Physics
School of Physical and Mathematical Sciences
Nanyang Technological University
637371, Singapore
Prof. Y. Luo
Department of Physics & Electronic Engineering
Xinyang Normal University
Xinyang 464000, P. R. China

DOI: 10.1002/adfm.201304206

core-shell nanowire arrays on Ti foils presented an improved capacitance (480 F g^{-1} at 2.67 A g^{-1}) for pseudo-capacitor with respect to that of pristine Co_3O_4 nanowire arrays. However, most of the previous researches on the Co_3O_4@MnO_2 composites are still focused on supercapacitors, and the capacitance and energy density are still very low. To the best of our knowledge, the Li-ion batteries application for Co_3O_4@MnO_2 is rarely explored.

Herein, we report a cost-effective and simple strategy to design and fabricate novel 3D hierarchical Co_3O_4@MnO_2 core-shell heterostructures directly grown on nickel foam as a binder-free electrode for high-performance electrochemical energy storage application, where the mesoporous Co_3O_4 acting as the "core" and ultrathin MnO_2 nanosheets working as the "shell" layer. This smart electrode design offers several advantages as follows: first, the selected Ni foam substrate with 3D network structure and increased surface area can provide ideal electron pathway and load more active materials per unit electrode area. Second, Co_3O_4 nanoneedles with well-defined single-crystalline nanostructure serve as both the backbone and conductive connection for MnO_2, and its porous feature can enlarge the specific surface area. Ultrathin nanosheets-like MnO_2 can increase the contact area with electrolyte, enable fast redox reaction, and protect the inner structure of Co_3O_4 as result of improving the durability. The synthesized 3D hierarchical Co_3O_4@MnO_2 core-shell structures are further investigated as anode material for both supercapacitors and Li-ion batteries applications, which exhibit excellent favorable electrochemical performance, such as high specific capacitance, high energy density and excellent long-term cycle stability in contrast to that of Co_3O_4 and MnO_2 individual component. Moreover, the morphologies control of Co_3O_4@MnO_2 and correlations between the electrochemical properties and the electrode morphology are discussed in detail.

2. Results and Discussion

2.1. Synthesis and Characterization

The fabrication processes of highly ordered Co_3O_4@MnO_2 NAs on the Ni foam are schematically illustrated in **Figure 1**. Typically, the $Co(OH)_2CO_3$ precursors were grown directly on nickel foam substrate via a facile modified hydrothermal synthesis process (step i); and further annealing enabled the formation of porous Co_3O_4 NAs (step ii); after that, the obtained porous nanoneedles were coated a thin carbon layer (step iii), which was purposely designed as an interfacial reactive template to grow MnO_2 nanosheets. Finally, Co_3O_4@MnO_2 NAs are obtained through the growth of MnO_2 nanosheets produced by the green reaction between $KMnO_4$ and graphitic carbon (step iv). The optical images of the Co_3O_4@MnO_2 NAs at different stage are provided in Figure S1, Supporting Information. As it can be seen, the color of the Ni foam surface turned into deep brown after the formation of MnO_2 nanosheets onto the Co_3O_4 NAs.

Figure 2a shows the SEM image of the as-synthesized well-ordered Co_3O_4 NAs. It can be seen that large-scale, dense and aligned Co_3O_4 nanoneedles grow uniformly on the skeletons of the Ni foam. The Co_3O_4 nanoneedles appear like numerous "grass", standing perpendicularly on the Ni foam substrate (Figure 2b). It is noting that each nanoneedle is made up of several nanoparticles, which are accumulated with each other, forming a highly porous structure. A careful examination (Figure 2d,f) reveals that these needle-like Co_3O_4 NAs are 6 μm in length and about 100 nm in diameter at the middle section. The SEM image of Co_3O_4 NAs taken at the damaged area as shown in Figure 2e further confirms the hybrid structures of Ni foam/Co_3O_4 nanoneedle arrays. After the MnO_2 growth, one layer of thin MnO_2 nanosheets is covered on the whole

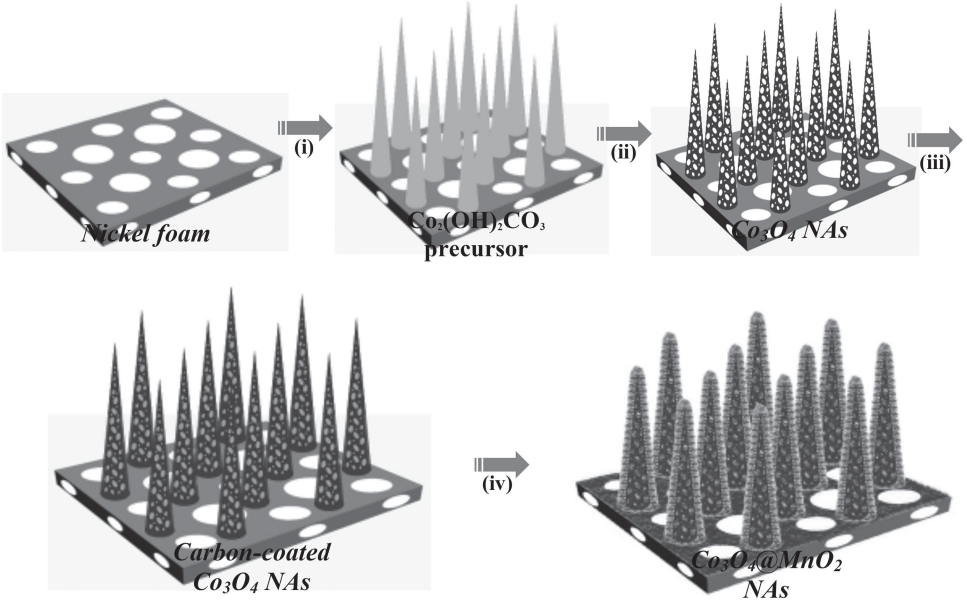

Figure 1. Schematic illustrating the fabrication processes of the Co_3O_4@MnO_2 NAs.

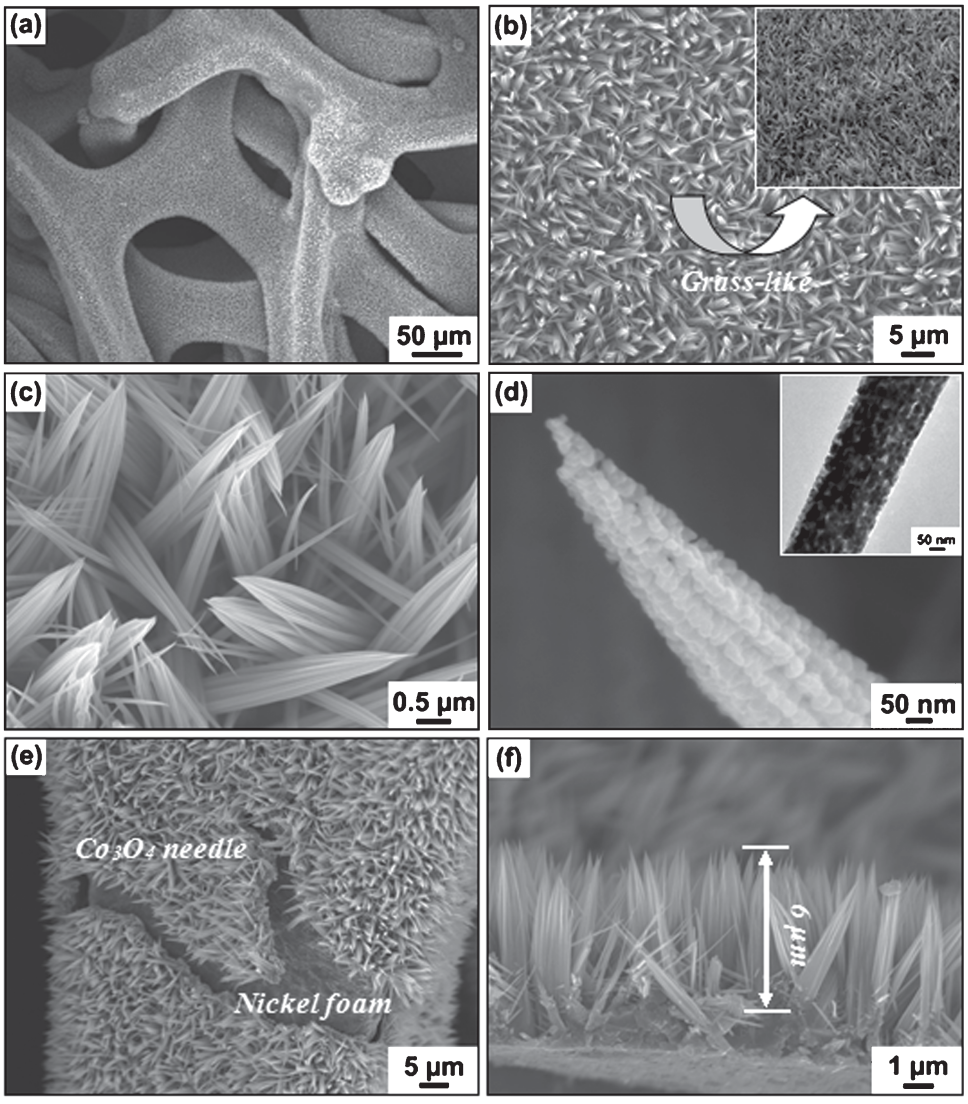

Figure 2. a–d) SEM images of Co_3O_4 NAs at various magnifications; e) SEM image of a cross-sectionally damaged Co_3O_4 NAs; f) Cross-sectional SEM image of Co_3O_4 NAs.

surface of each Co_3O_4 nanoneedle, forming a core-shell hierarchical structure (as shown in **Figure 3**). From the high magnification SEM images (inset of Figure 3b,d), it can be found that the MnO_2 nanosheets with thickness of ≈5 nm are interconnected with each other but still not fully covering the entire core, keeping a highly porous configuration. The pores or voids between the nanosheets and nanoneedles of both the core and shell are beneficial to the electrolyte infiltration, and the interconnected structures allow fast ion and electron transportation. The cross-sectional SEM image (Figure 3e) indicates that the MnO_2 nanosheets are homogeneously covered the whole surface of the Co_3O_4 nanoneedles. The TEM observation (Figure 3f) further demonstrates the uniformity coverage of the MnO_2 nanosheets, and the thickness of MnO_2 nanosheets layer is about 200 nm.

More detailed structural information and morphology evolution of the Co_3O_4@MnO_2 NAs were investigated by transmission electron microscopy (TEM) and selected area electron diffraction (SAED). The typical TEM images of Co_3O_4 nanoneedles in **Figure 4**a,b show that the Co_3O_4 nanoneedles are consisted of nanoparticles with the diameter gradually decrease from the root to the tip. The measured lattice spacing of 0.24 nm in HRTEM image of Figure 4c is corresponding to the (242) planes of cubic Co_3O_4. The SAED pattern of the Co_3O_4 nanoneedle shows a set of well-defined spots, indicative of its single-crystallinity property. The TEM images taken from the Co_3O_4@MnO_2 NAs confirms the core-shell hierarchical structure with the Co_3O_4 nanoneedle as a core part and MnO_2 nanosheets as a shell layer. HRTEM observation and SAED in Figure 4f also confirm that the MnO_2 nanosheets are crystalline structure.

The chemical compositions and metal oxidation states of the Co_3O_4@MnO_2 NAs are analyzed by X-ray photoelectron spectroscopy (XPS) (as shown in Figure S2, Supporting Information). A full-survey-scan spectrum in Figure S2a (Supporting Information) indicates the presence of Co, O, and Mn elements

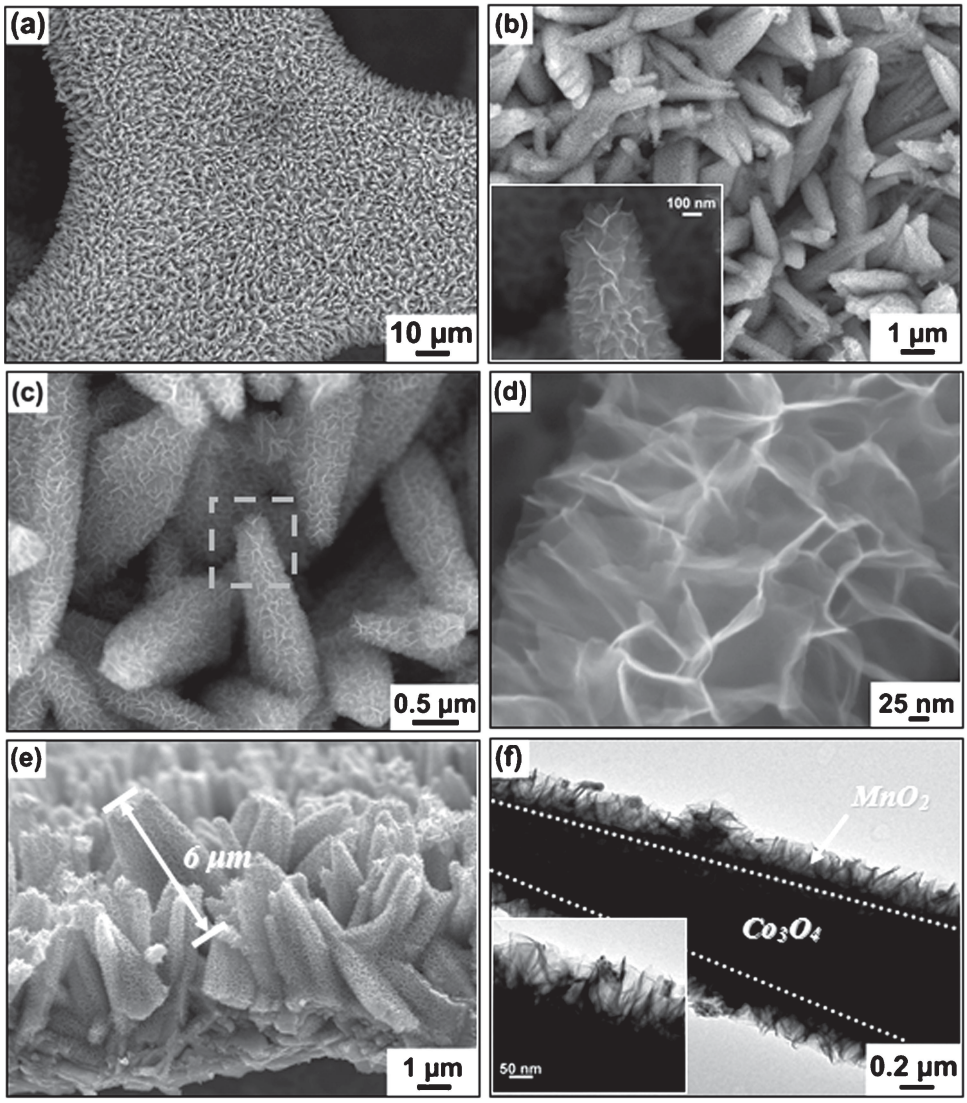

Figure 3. a–d) SEM images of Co_3O_4@MnO_2 NAs at various magnifications; e) Cross-sectional SEM image of Co_3O_4@MnO_2 NAs; f) Low-magnification TEM image of Co_3O_4@MnO_2 NAs.

in the Co_3O_4@MnO_2 NAs. Two major peaks with binding energies at 780.3 and 795.7 eV are observed by deconvolution of complex Co 2p curve (Figure S2b, Supporting Information), corresponding to the Co $2p_{1/2}$ and Co $2p_{3/2}$ spin-orbit peaks, respectively. The deconvolution peaks (as shown in Figure S2c, Supporting Information) of the O 1s spectrum are also resolved into two components, centered at 530 and 531.3 eV, respectively. The low binding energy component observed at 530 eV is attributed to the O^{2-} forming oxide with cobalt and manganese elements, the latter peak is assigned to the OH^-.[22] The XPS spectra of Mn 2p region (Figure S2d, Supporting Information) displays two distinct peaks at binding energies of 641.9 and 653.1 eV originating from the Mn $2p_{3/2}$ and Mn $2p_{1/2}$ spin-orbit peaks, respectively, indicating that the elemental Mn is in the chemical particles exists as Mn^{4+}.[38]

The phase and structures of as prepared Co_3O_4 nanoneedles, MnO_2 nanosheets and Co_3O_4@MnO_2 NAs on the Ni foam were verified by powder X-ray diffraction (XRD) and Raman spectrum. As shown in **Figure 5**a, the diffraction peaks can be well indexed with cubic phase Co_3O_4 (JCPDS card no. 42–1467) and birnessite-type MnO_2 (JCPDS card no. 50–0866), respectively.[39,40] The three strongly peaks marked by "#" belong to the Ni substrate. The structural features of the Co_3O_4@MnO_2 nanocomposites were further confirmed using Raman measurements. As shown in Figure 5b, the peaks detected at around 480 cm^{-1}, 525 cm^{-1}, 615 cm^{-1}, and 682 cm^{-1} are assigned to the E_g, F^1_{2g}, F^2_{2g}, and A_{1g} modes of Co_3O_4.[41] While the three Raman bands located at 501, 575, and 645 cm^{-1} are in good agreement with the three major vibrational features of the birnessite-type MnO_2 compounds.[42]

2.2. The Morphology Evolution and Growth Mechanism

The evolution process of Co_3O_4 nanostructures with varied temperature and times are investigated in detail. We found that

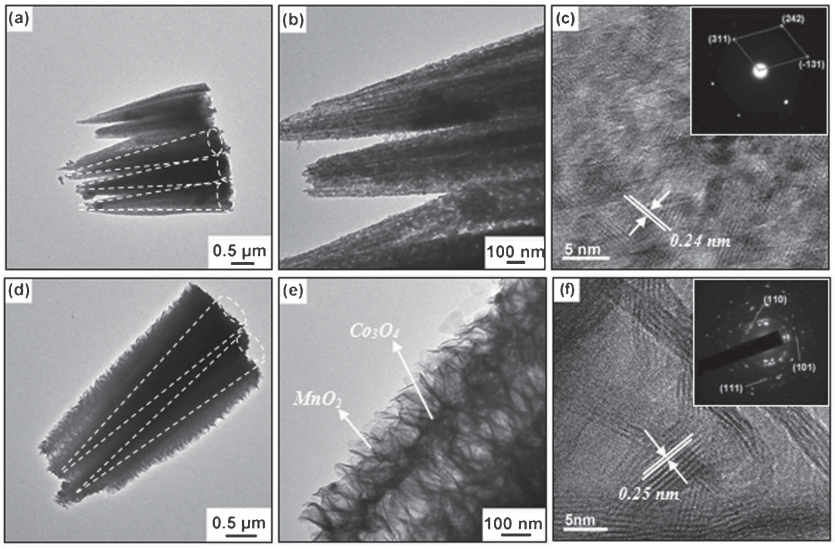

Figure 4. Low-magnification and high-magnification TEM images of a–c) the Co_3O_4 NAs; d–f) Co_3O_4@MnO_2 NAs. The insets of (c,f) are the corresponding SAED patterns from Co_3O_4 NAs and Co_3O_4@MnO_2 NAs.

the growth temperature played an important role in the morphology of Co_3O_4. With a lower growth temperature of 80 °C, the morphology of as-obtained products are mainly nanosheets, due to the lower interfacial nucleation energy on the substrate, as shown in **Figure 6**a,b. With the temperature increase to 100 °C, nanosheets-nanoneedles hybrid structures are obtained (Figure 6d). It is evident that the sample structure is derived from a Co_3O_4 nanosheet, which gives birth to multi-directional nanoneedles at the top of the nanosheets (inset of Figure 6c), and the nanoneedles are aggregated to form a cluster arrays. This morphology change might be due to that the concentrations of CO_3^{2-} and OH^- increased under a high temperature by the hydrolysis-precipitation of urea, which is beneficial to form nanoneedle structures. When the temperature is above 120 °C, Co_3O_4 mainly tended to grow into needle or wire-like nanostructures. Figure 6e,f shows the morphology of nanoneedles grown at 120 °C. These nanoneedles were intercrossed and interconnected with one another, forming an intricate transportation network. As shown in inset of Figure 6e, the nanostructures are typically about 6 μm length and 50–100 nm in diameter. When the synthesis process was carried out at a higher temperature (160 °C), slender and thick Co_3O_4 nanowires were obtained (Figure 6g,h). Noting that all the Co_3O_4 nanostructures prepared at different growth temperature are cubic phase as evidenced by XRD (Figure S2, Supporting Information). As can be seen in Figure 6i–l, Co_3O_4@MnO_2 core–shell nanostructure arrays with different morphology have been fabricated base on Co_3O_4 nanostructure arrays after hydrothermal treatment for 12 h with temperature varying from 80 °C to 160 °C. After the MnO_2 growth, the surface of Co_3O_4 was homogeneously covered with a layer of dense MnO_2 ultrathin nanosheets, resulting in a highly porous surface morphology. The proposed growth mechanism can be summarized in Figure 6m. The evolution of Co_3O_4 NAs with varied times was studied by observing the sample morphology taken at different stages (Figure S4a–d, Supporting Information). In the beginning, the Ni foam

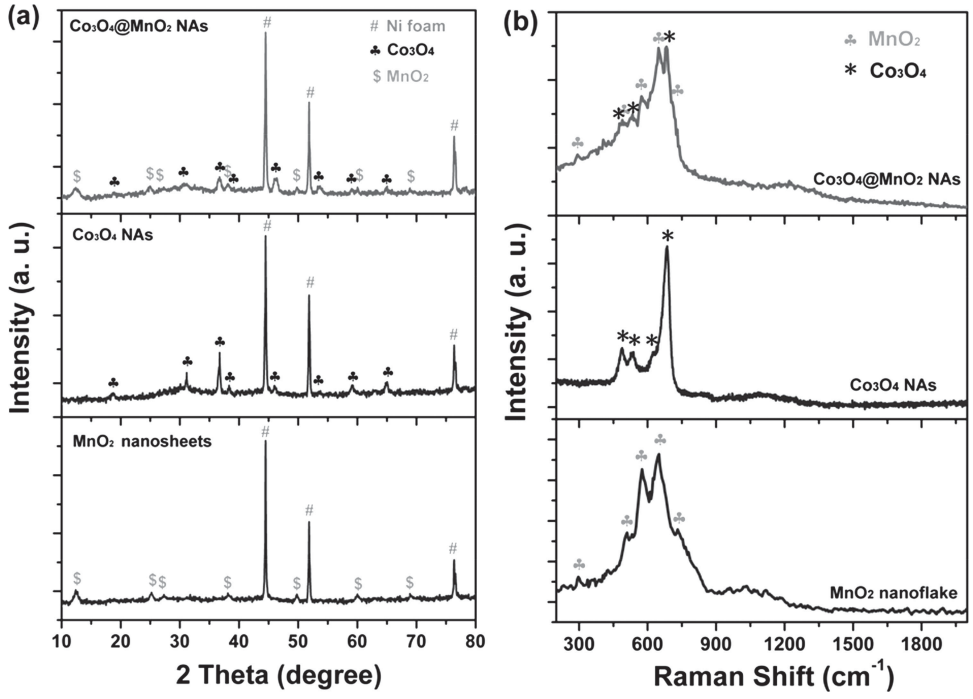

Figure 5. a) XRD patterns and b) Raman spectra of Co_3O_4@MnO_2 NAs, Co_3O_4 NAs, and MnO_2 nanosheets.

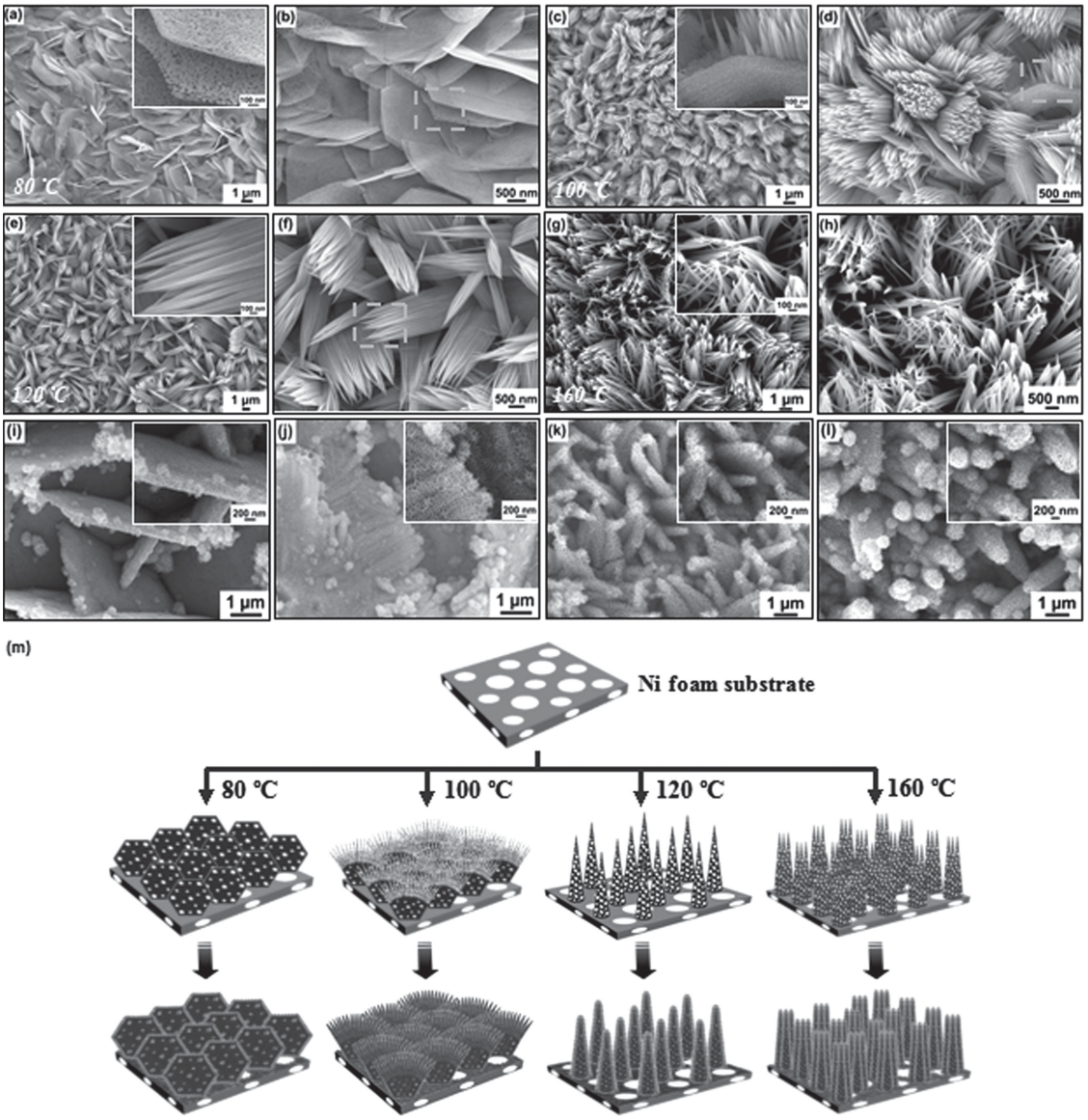

Figure 6. Temperature-dependent evolution of the Co_3O_4 arrays nanostructures at different hydrothermal reaction temperature: a,b) 80 °C, c,d) 100 °C, e,f) 120 °C, and g,h) 160 °C. i–l) The SEM images of Co_3O_4@MnO_2 core/shell nanostructure arrays fabricated base on Co_3O_4 nanostructure arrays after hydrothermal treatment for 12 h with temperature varying from 80 °C to 160 °C. m) Proposed mechanism for the effect of temperature on the morphology construction.

shows rough surface after acid treatment, after 3 h hydrothermal growth, unique hybrid structures with multiple directions of secondary needle-like nanowires grown on the major nanosheets were observed on the Ni foam, when the reaction time was further prolonged to 6 h, the small flakes turned into bigger sheets with tiny needles. Subsequently, nanosheets completely disappeared, only needle-like nanowires on the Ni foam could be obtained. The effects of growth conditions like times and carbon layer thickness on the morphology of MnO_2 were also studied, the detailed information can be found in Figures S4,S5 (Supporting Information). As shown in Figure S4e–h, at the early stage, one can see that the core nanoneedles surface become rough, decorated by many tiny MnO_2 "buds", which distinctly indicates that the MnO_2 shell begins to grow on the surface of the Co_3O_4 nanoneedles. With the reaction time was gradually prolonged, the ultrathin MnO_2 nanoflakes formed uniformly on the nanoneedle surface and the thickness of the nanoflakes decreases accordingly. The thickness of the MnO_2 shell can be easily controlled by changing the hydrothermal reaction times. The corresponding mechanism for the effect of growth times on morphology is proposed, as shown in Figure S4i, Supporting Information. For the MnO_2 growth, glucose plays an essential role in providing the uniform coating of an amorphous carbon layer on the nanoneedle surface, resulting in the formation of this sort of morphology. As shown in Figure S5 (Supporting Information), with the increasement of glucose concentrations, more MnO_2 nanoballs can be derived from Co_3O_4@MnO_2 NAs. Moreover, MnO_2 nanosheets on Ni foam

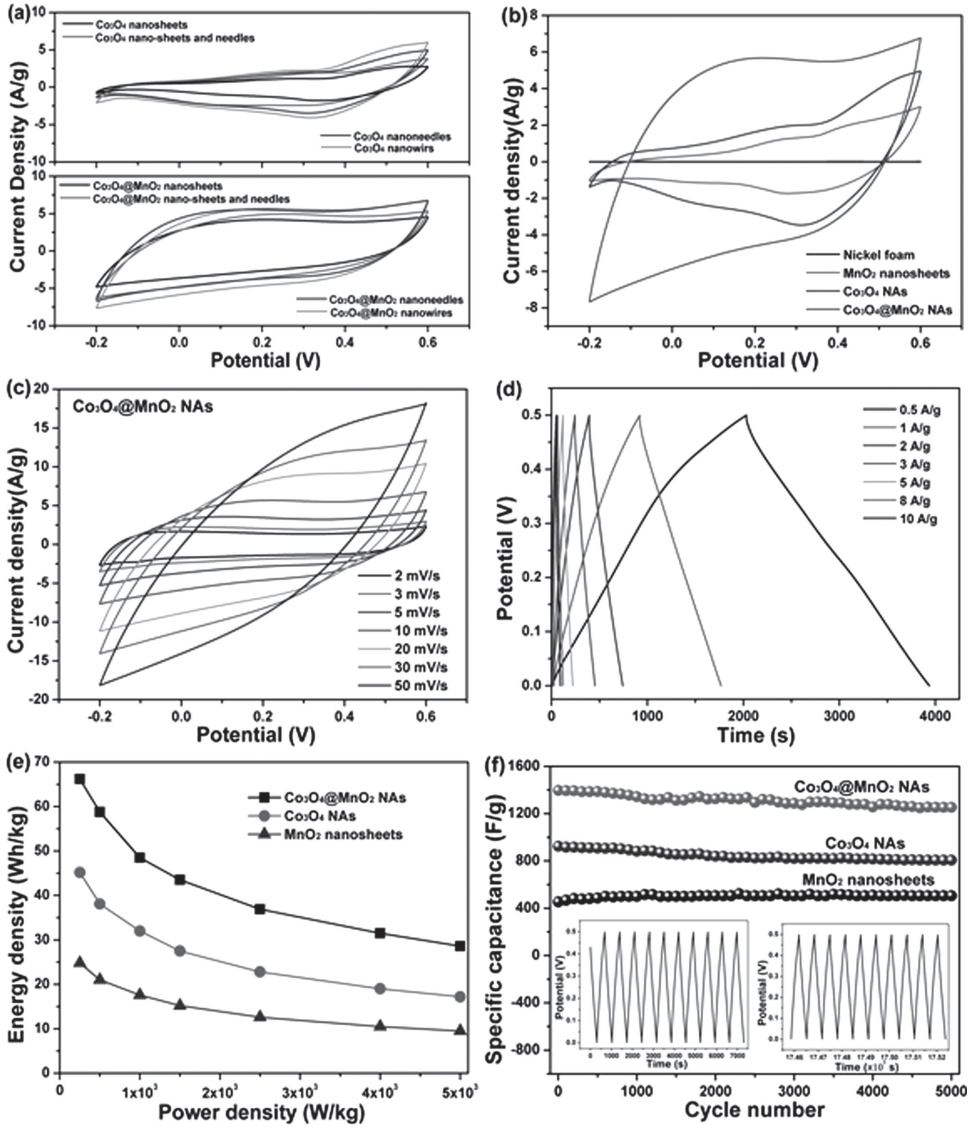

Figure 7. a) CV curves of the Co_3O_4 and Co_3O_4@MnO_2 nanostructure arrays prepared at different temperature. b) CV curves for Ni foam, MnO_2 nanosheets, Co_3O_4 NAs and Co_3O_4@MnO_2 NAs, recorded at a scan of 10 mV s^{-1}; c,d) CV and galvanostatic charge–discharge curves of the Co_3O_4@MnO_2 composites at different scan rates and different current density in 1 M LiOH aqueous solution, respectively; e) Ragone plots of Co_3O_4@MnO_2 NAs electrode, Co_3O_4 NAs electrode, and MnO_2 nanosheets electrode; f) Cycling performance of the MnO_2 nanosheets, Co_3O_4 NAs and Co_3O_4@MnO_2 NAs electrodes (5000 cycles). The inset shows the charge-discharge curves.

were also prepared for reference (as shown in Figure S6, Supporting Information).

2.3. Electrochemical Evaluation of Supercapacitors

The electrochemical storage application of as-prepared products is evaluated by testing them as elecrodes for supercapacitors. First, the correlation relationship between the morphology and capacitive property is discussed. **Figure 7**a depicts a comparison on the cyclic voltammetric (CV) curves of Co_3O_4 nanosheets, Co_3O_4 nanosheets-nanoneedles, Co_3O_4 nanoneedles and Co_3O_4 nanowires that prepared under different temperature. The tests were carried out in a three-electrode system at a scan rate of 10 mV s^{-1} with 1 M LiOH electrolyte at a potential sweep window of –0.2 to 0.6 V. The shape of curves is slightly deviated from ideal rectangular voltammogram indicating the pseudocapacitive behavior of cobalt oxides. As seen in the voltammograms, the curves' area of electrodes gradually increase along with the increase the growth temperature under the same measure condition, indicating that the Co_3O_4 nanowires under 160 °C give the highest capacity. This might be due to the fact that the Co_3O_4 nanowire structures process the largest surface area in contrast to that of nanosheets and nanoneedle structures. After the MnO_2 growth, although the enclosed area of Co_3O_4 nanoneedles@MnO_2 nanosheets and Co_3O_4 nanowires@MnO_2 nanosheets hierarchical structures are almost the same at a small scan rate (10 mV s^{-1}), the former is obviously

better than the latter at larger scan rate (more than 10 mV s^{-1}) (as shown in Figure S7, Supporting Information), which suggesting the Co_3O_4 nanoneedles@MnO_2 nanosheets is the optimal electrode design due to their high surface area plus effective porosity. In addition, Figure S8a (Supporting Information) shows the CV curves of the hierarchical Co_3O_4@MnO_2 arrays obtained at different concentrations of glucose, while the enclosed area of the Co_3O_4@MnO_2 NAs obtained at 0.04 M glucose is the largest in the three samples. So the following performance tests were focused on the Co_3O_4 nanoneedles@MnO_2 nanosheets arrays.

The CV curves of the pristine Ni foam, MnO_2 nanosheets, Co_3O_4 NAs and Co_3O_4@MnO_2 NAs electrode at a scan rate of 10 mV s^{-1} are shown in Figure 7b. It can be found that the capacitance contribution from Ni foam substrate is negligible. The current density and enclosed CV curve area of the Co_3O_4@MnO_2 NAs are much larger than that of the individual Co_3O_4 nanoneedles or MnO_2 nanosheets, arising from the increased surface area and hybrid structural effect from the ultrathin MnO_2 nanosheets and Co_3O_4 nanoneedles. The rate capability of Co_3O_4@MnO_2 NAs electrodes was also investigated by measuring the CV curves at different scan rates and charging-discharging curves at different current densities, respectively. As shown in Figure 7c, although the shapes of the CV curves deviate from ideal rectangular shape, the areas surrounded by the CV curves are not significantly influenced by the change in scan rates, implying good charge-discharge properties and rate capability of the Co_3O_4@MnO_2 NAs electrode, which demonstrate an improved rate capability in contrast to that of Co_3O_4 NAs electrode (Figure S8b, Supporting Information). The galvanostatic charge-discharge curves of Co_3O_4@MnO_2 NAs tested at current densities of 0.5–10 A g^{-1} are shown in Figure 7d. It can be seen that each curve has a good symmetry and fairly linear slopes, indicating a good electrochemical capacitive characteristic and superior reversible redox reaction. The specific capacitance can be calculated from the discharge curves according to the above mentioned equations (Equation 7). The specific capacitance of the Co_3O_4@MnO_2 NAs at 0.5, 1, 2, 3, 5, 8, and 10 A g^{-1} can be calculated to be 1905.4, 1693.2, 1396, 1253.4, 1062, 905.6, and 823 F g^{-1}, respectively. The specific capacitances of the three electrodes derived from the discharging curves at different current densities were compared, as shown in Figure S8e. The Co_3O_4@MnO_2 NAs electrode delivered a specific capacitance of 1693.2 F g^{-1} at the current density of 1 A g^{-1}, which was much higher than that of the Co_3O_4 NAs electrode (1096.4 F g^{-1}) or MnO_2 nanosheets electrode (603.2 F g^{-1}). In addition, at a high current density of 10 A g^{-1}, the Co_3O_4@MnO_2 NAs electrode still delivered a high specific capacitance of 823 F g^{-1}, indicating its superior rate capability. The CV and charge-discharge results from Co_3O_4 NAs and MnO_2 nanosheets electrodes are provided in Figure S8b,c (Supporting Information). The power density and energy density are two key parameters for supercapacitors in practical application. The Ragone plots of the Co_3O_4@MnO_2 NAs, Co_3O_4 NAs, and MnO_2 nanosheets electrodes are shown in Figure 7e. At a power density of 0.25 kW kg^{-1}, the Co_3O_4@MnO_2 NAs deliver an energy density of 66.2 W h kg^{-1}, which is much higher than that of the Co_3O_4 NAs (45.2 W h kg^{-1}) and MnO_2 nanoflakes (24.8 W h kg^{-1}), respectively. Even at a high power density of 5 kW kg^{-1}, the energy density of the Co_3O_4@MnO_2 NAs can reach 28.6 W h kg^{-1}, and is still larger than that of the Co_3O_4 NAs (17.2 W h kg^{-1}) and MnO_2 nanosheets (9.5 W h kg^{-1}). Moreover, the internal resistance (IR) of the Co_3O_4@MnO_2 NAs electrode (the IR drop is 0.006 V) was significantly reduced compared to that of the Co_3O_4 NAs electrode (the IR drop is 0.021 V) and MnO_2 nanosheets electrode (the IR drop is 0.012 V) (Figure S8d, Supporting Information).

The long-term cycle stability of supercapacitors is another critical issue in practical use. The cycling lifetime tests over 5000 cycles for the hybrid Co_3O_4@MnO_2 NAs, pristine Co_3O_4 NAs, and MnO_2 nanosheets were carried out at 2 A g^{-1}. As depicted in Figure 7f, it is found that the hybrid Co_3O_4@MnO_2 NAs electrode exhibits an excellent long-term electrochemical stability, and the capacitance loss after 5000 cycles is only 10.2%. By contrast, only 79.1% capacitance was retained for the pristine Co_3O_4 NAs. Importantly, the charge-discharge curves are still keeping quite symmetric after 5000 cycles test, indicating that there are no significant structural changes of the Co_3O_4@MnO_2 NAs electrode during the charge/discharge processes. Such excellent cycling stability is mainly attributed to the porous configuration of the Co_3O_4 core, which can not only lead to more contact area with the electrolyte, but also can accommodate the possible volume change during cycling process. More significantly, the synergist effect between MnO_2 and Co_3O_4 may inhibit the anodic dissolution of MnO_2, and consequently improve the electrochemical reversibility and stability of the hybrid electrode.

2.4. Electrochemical Evaluation of Lithium-Ion Batteries

As both Co_3O_4 and MnO_2 are active lithium-ion batteries anode materials, the Co_3O_4@MnO_2 NAs are also tested as anode for lithium-ion batteries (LIBs). **Figure 8**a shows the first three CV curves of Co_3O_4@MnO_2 NAs and Co_3O_4 NAs at room temperature in the range of 0.01–3.0 V versus Li/Li^+ at a slow scan rate of 0.5 mV s^{-1}. Based on the previously reported storage mechanism of MnO_2 and Co_3O_4,[43,44] the lithium insertion and extraction reactions can be expressed as follows:

$$4Li \leftrightarrow 4Li^+ + 4e^-$$

$$MnO_2 + 4Li^+ + 4e^- \leftrightarrow 2Li_2O + Mn$$

$$Co_3O_4 + 8Li^+ + 8e^- \rightarrow 4Li_2O + 3Co$$

$$Co + Li_2O \leftrightarrow CoO + 2Li^+ + 2e^-$$

As can be seen, a strong irreversible cathodic peaks located around 0.48 V in the first cycle corresponds to the electrochemical lithium insertion reaction (Equation 2), which can be attributed to the formation of Li_2O and Mn. Meanwhile, the subsequent well-defined anodic peaks are observed at 1.65 V and 2.30 V, indicating the extraction of Li^+ in the electrode materials (Equations 1,4). The subsequent cycles differ slightly from the first one, indicating different redox behavior. The reduction peaks shift to 0.86 V and a shoulder peak at about 2.15 V is observed, which can be attributed to the formation of Li_2O and

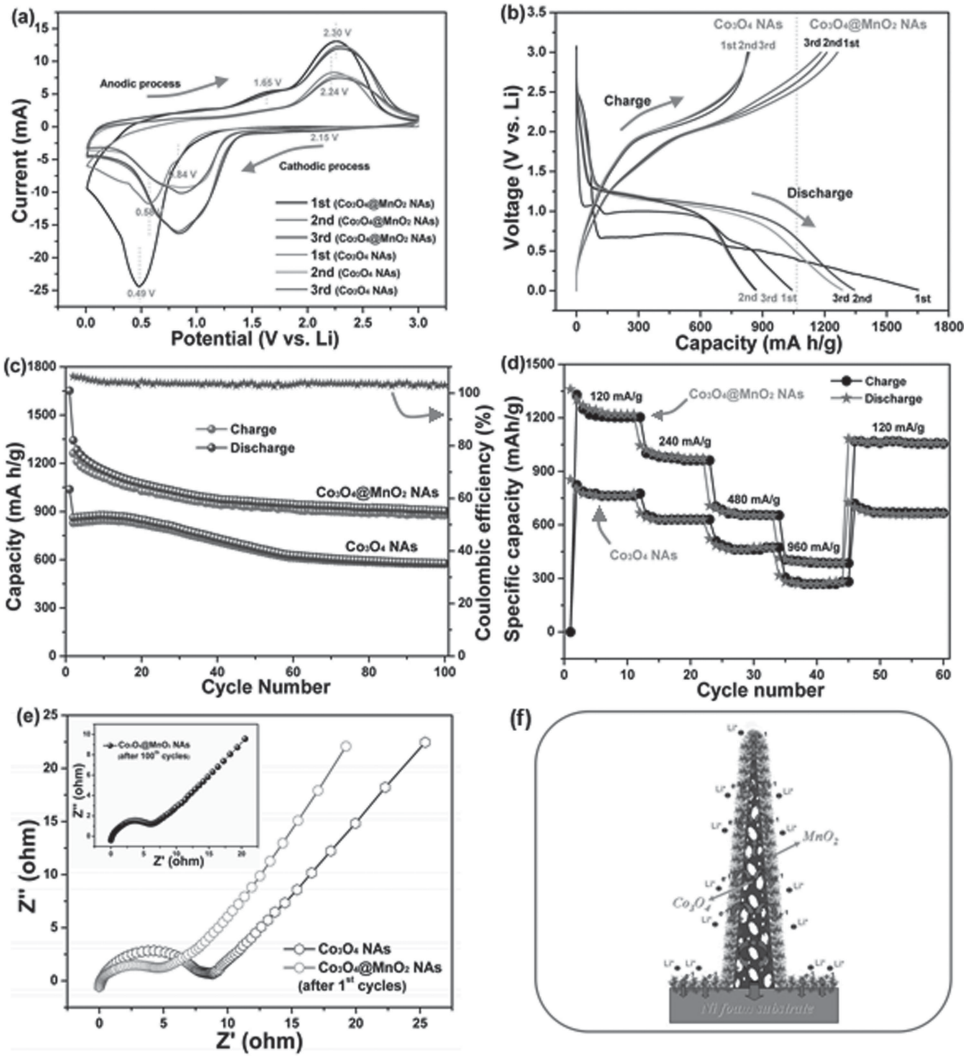

Figure 8. Electrochemical characterization of lithium-ion batteries: a) CV curves of the electrodes at a scan speed of 0.5 mV s^{-1} in the voltage of 0.01–3.0 V vs Li; b) Galvanostatic discharge/charge profiles of the Co_3O_4@MnO_2 NAs anode at a constant current density of 120 mA g^{-1} for the 1st, 2nd, 3rd, 10th, 20th, 30th, 50th, and 100th; c) Reversible capacity vs current density (rate capability) for different anodes; d) Cycling performance of the both the two electrodes at a constant current density of 120 mA g^{-1}; e) Electrochemical impedance spectra after the 1st cycles of the Co_3O_4 NAs and Co_3O_4@MnO_2 NAs anode (inset: electrochemical impedance spectra after the 100th cycle of the Co_3O_4@MnO_2 NAs anode); f) Schematic representation of rechargeable lithium-ion battery based on Co_3O_4@MnO_2 NAs on Ni foam.

Co (Equations 3,4) due to the electrolyte further dip into the internal of electrode materials. It is worthy noting that the CV peaks overlap well during the subsequent cycles. This means that the electrochemical reaction becomes highly reversible after the first discharge-charge. As shown in Figure 8b, the discharge–charge voltage–capacity profiles show two voltage plateaus at 0.52 and 0.68 V in the first cycle, which correspond to irreversible reactions, and the voltage plateaus are not observed in the second cycle, in agreement with the CV results. The Co_3O_4@MnO_2 NAs electrode presents a high initial capacity of 1652.3 mAh g^{-1} and a lower capacity of 1262.3 mAh g^{-1} in the second cycle, resulting in a first-cycle columbic efficiency of around 76.4%. The capacity loss is most likely due to the irreversible reactions by the formation of the solid electrolyte interface (SEI) layer, as seen also from the shape difference between the discharge voltage profiles of the first and second cycle.[45,46] The cyclic voltammograms and voltage-capacity trace of Co_3O_4 NAs reference were also measured and provided in Figure 8a,b for comparison.

The capacity versus cycle number plot is shown in Figure 8c. As can be seen, it is evident that the Co_3O_4@MnO_2 NAs electrode exhibits exceptional cyclability. The capacity decreases gradually in the first 40 cycles, and stabilizes at around ≈924 mA h g^{-1} in the following 60 cycles. The capacity enhancement can be mainly attributed to one reason that along the increase of cycle numbers, more reacting sites of Co_3O_4@MnO_2 NAs have been activated, participating in the lithium-ion storage and making contribution to the final capacity. For a better understanding of the rate performance of the Co_3O_4@MnO_2 NAs in lithium energy storage, the discharge and charge cycles of the cell is performed at different current densities and subsequent cycling at 120 mA g^{-1}, as

shown in Figure 8d. Irreversible capacity losses during the initial two cycles are observed for the electrodes presumably due to decomposition of the electrolyte and/or solvent. Nevertheless, the first discharge capacity of ≈1220 mA h g^{-1} for the Co_3O_4@MnO_2 NAs is much higher than those of the Co_3O_4 NAs (≈763 mA h g^{-1}). Subsequently, the current density is increased stepwise to 240 mA g^{-1}, the specific capacity of the Co_3O_4@MnO_2 NAs is ≈982 mA h g^{-1}, which is slowly reduced to ≈675 mA h g^{-1} at 480 mA g^{-1} and ≈387.5 mA h g^{-1} at 960 mA g^{-1}, respectively. After 45 cycles, with the current rate being again decreased back to 120 mA g^{-1}, a capacity of ≈1060 mA h g^{-1} can be recovered. These capacities are also higher than that of the Co_3O_4 NAs electrode under the same conditions. The excellent rate performance and cyclability render the Co_3O_4@MnO_2 NAs very promising candidate for LIBs application.

To gain further insight into the advantages of these electrodes, impedance spectra of the pristine Co_3O_4 NAs and Co_3O_4@MnO_2 NAs composite after the 1st cycle were measured in the frequency range from 0.01 Hz to 100 kHz at an open circuit potential with an AC perturbation of 5 mV (as shown in Figure 8e). The result shows that the Nyquist plots are in the form of an arc at the high frequency region and a straight ≈45° sloped line at low frequency region. The arc in the high frequency region is associated with the interfacial properties of the electrodes and corresponds to the charge transfer resistance, and the straight line in the low frequency region is ascribed to the diffusive resistance related to the diffusion of the electrolyte within the pores of the electrode. It is obvious that both the Co_3O_4@MnO_2 NAs and the pristine Co_3O_4 NAs have similar diffusion resistance, but the Co_3O_4@MnO_2 NAs demonstrate a relatively smaller charge transfer resistance. As shown in the inset of Figure 8e, the arc increment from the 1st to the 100th cycles is not so obvious indicating that the Co_3O_4@MnO_2 NAs nanostructures are well maintained and preserved overall with little structural deformation after 100 cycles.

These test results of LIBs reveal a high specific capacity, excellent cycling stability, and outstanding rate performance of the Co_3O_4@MnO_2 NAs electrode, which can be mainly ascribed to the hierarchical 3D composite structures and a direct growth on a conductive substrate. As schematically demonstrated in Figure 8f, the unique 3D core-shell hierarchical configuration has an increased portion of exposed surface, which provides more active sites for Li^+ ions access and accommodates the stress induced by the volume change during the electrochemical reaction, thus leading to a higher efficiency of the lithiation and delithiation process. The porosity on the surface further shortens the diffusion paths for lithium ions and enhances the rate capability. Moreover, direct growth on Ni foam can form good adhesion and a better electrical contact between Co_3O_4 NAs and the substrate.

3. Conclusion

In summary, we have demonstrated the rational design and fabrication of the 3D hierarchical Co_3O_4@MnO_2 core-shell nanoneedle arrays through a stepwise, seed-assisted hydrothermal approach. These results show that the obtained hierarchical nanostructure exhibits outstanding advantages in electrochemical energy storage. This smart electrode made of Co_3O_4@MnO_2 core–shell nanoneedle arrays exhibit excellent electrochemical performance both in supercapacitors and Li-ion batteries in the terms of specific capacity, cycling lifespan and rates stability, which are much better than that of the individual part, owing to that each component provides a much needed critical function for the efficient use of the metal oxide for energy storage, which could be the most important factor in realizing the synergetic effect between the two pseudocapacitive oxides, that is, porous Co_3O_4 nanoneedle arrays and ultrathin MnO_2 nanosheets. Moreover, the 3D Ni foam substrate can increase the surface area of the active electrode materials, and thus help to further improve the overall energy density. Our work not only opens up the possibility to engineer cobalt oxides and MnO_2 into promising electrode materials but also presents a facile and affordable general approach to design hybrid electrode architectures for energy storage devices.

4. Experimental Section

Synthesis of Mesoporous Co_3O_4 NAs on Nickel Foam: All the purchased chemicals were analytical grade and used without further purification. In a typical process, 0.58 g of $Co(NO_3)_2 \cdot 6H_2O$ was dissolved into 40 mL of deionized water at room temperature to form a homogeneous pink solution, then 0.30 g of NH_4F and 0.60 g of urea were added, respectively. One piece of Ni foam (2 cm × 4 cm in rectangular shape) was immersed in a 3 M HCl solution in an ultrasound bath for 15 min to remove the possible surface oxide layer, and then rinsed with deionized water and absolute ethanol several times. After that, the above prepared aqueous solution and the pre-treated Ni foam were transferred into a 50 mL Teflon-lined stainless-steel autoclave, which was sealed and maintained at 120 °C for 9 h, and then cooled down to ambient temperature naturally. Finally, the product was taken out, washed, vacuum dried and then thermally treated at 400 °C in air for 4 h to get crystallized Co_3O_4 nanoneedle arrays. The reactions involved were illustrated as follows.

$$Co^{2+} + xF^- \rightarrow [CoF_x]^{(x-2)-}$$

$$H_2NCONH_2 + H_2O \rightarrow 2NH_3 + CO_2$$

$$CO_2 + H_2O \rightarrow CO_3^{2-} + 2H^+$$

$$NH_3 \cdot H_2O \rightarrow NH_4^+ + OH^-$$

$$2[CoF_x]^{(x-2)-} + CO_3^{2-} + 2OH^- + H_2O \rightarrow Co_2(OH)_2CO_3 \cdot nH_2O + 2xF^-$$

During the annealing process:

$$3Co_2(OH)_2CO_3 \cdot nH_2O + O_2 \xrightarrow{\Delta} 2Co_3O_4 + 3(n+1)H_2O + 3CO_2$$

The Co_3O_4 nanoneedle arrays consist of numerous interconnected nanoparticles and presents a rough surface with a large quantity of mesoporous structures, which is ascribed to the successive release and loss of CO_2 and H_2O during the thermal decomposition of $Co_2(OH)_2CO_3$ precursor (the heating process is marked by "Δ").

Preparation of 3D Co_3O_4@MnO_2 NAs on Nickel Foam: 3D Co_3O_4@MnO_2 hierarchical structures were prepared by growth MnO_2 nanosheets onto the Co_3O_4 nanostructure backbones with a carbon-assisted reaction process. First, self-supported Co_3O_4 nanostructure arrays were modified by one thin layer of carbon. In a typical process: a piece of Co_3O_4/Ni foam substrate was first immersed into a 0.04 M aqueous glucose solution for 24 h, followed by carbonization at 450 °C in Ar gas for 2 h. After that, the carbon modified Co_3O_4 was put into a Teflon-lined stainless steel autoclave containing a 0.03 M $KMnO_4$ solution, which was subsequently maintained at 160 °C for 1–5 h. Finally, the sample was removed out, washed with distilled water, and dried at 60 °C to obtain a hierarchical Co_3O_4@MnO_2 nanostructure arrays. For comparison, the bare MnO_2 films growth on Ni foam were also obtained using a similar approach.

Materials Characterizations: The morphology of the samples was characterized using a field-emission scanning electron microscope (SEM) (JEOL JSM 6700F, Japan) operating at 20 KV. The phase purity of the products was characterized by X-ray powder diffraction (XRD) using a D8 Focus (Germany, Bruker) automated X-ray diffractometer system with Cu-Kα (λ = 1.5406 Å) radiation at 40 kV and 40 mA in a 2 range from 20° to 80° at room temperature. Transmission electron microscopy (TEM) and high-resolution TEM (HRTEM) observations were recorded on a JEOL JEM-2010 instrument in bright field and on a HRTEM JEM-2010FEF instrument (operated at 200 kV). Raman spectroscopy was carried out using WITEC CRM200 Raman system equipped with a 532 nm laser source and 100× objective lens. X-ray photoelectron spectroscopy (XPS) spectra were measured on a Perkin-Elmer model PHI 5600 XPS system with a resolution of 0.3–0.5 eV from a monchromated aluminum anode X-ray source.

Supercapacitor Performance Measurements: The electrochemical measurements were performed on an electrochemical workstation (CHI 660D, CH Instruments Inc., Shanghai) using a three-electrode mode in 1 M LiOH aqueous solution within the potential window of approximately –0.2 to 0.6 V. The Co_3O_4@MnO_2 hybrid or pristine Co_3O_4 NAs ($S_{Co3O4@MnO2} \approx$ 1 cm × 3 cm; $m_{Co3O4} \approx$ 3.0 mg, $m_{MnO2} \approx$ 2.0 mg) was directly used as the working electrode. A Pt plate and Ag/AgCl were used as the counter electrode and the reference electrode, respectively. EIS measurements were performed by applying an AC voltage with 5 mV amplitude in a frequency range from 0.01 Hz to100 kHz. The specific capacitance (C), energy density (E in W h kg^{-1}) and power density (P in kW kg^{-1}) were calculated according to the following equations:

$$C = \frac{I \times \Delta t}{m \times \Delta V}$$

$$E = \frac{1}{2 \times 3.6} \times C \times \Delta V^2$$

$$P = \frac{E}{\Delta t}$$

where I (mA) is the constant discharge current, m (mg) is the mass of the active materials, ΔV (V) is the potential drop during discharge, Δt (s) is the discharge time. The specific capacitance (F g^{-1}) and current density (A g^{-1}) were calculated based on the mass of two active materials, that is, Co_3O_4 and MnO_2.

Battery Performance Measurements: The cells were assembled in an Ar-filled glovebox (Mbraun, Unilab, Germany) by directly using the Co_3O_4@MnO_2 NAs ($m_{Co3O4+MnO2} \approx$ 2.4 mg; m_{Co3O4} : m_{MnO2} = 1.5 : 1), Co_3O_4 NAs ($m_{Co3O4} \approx$ 1.2 mg) as the working electrode, a Li-metal circular foil (0.59 mm thick) as the counter and reference electrodes, a microporous polypropylene membrane as the separator, and a solution of 1 M $LiPF_6$ in ethylene carbonate (EC)/diethyl carbonate (DEC) (1 : 1 by volume) was used as electrolyte. The cells were aged for 15 h before the measurements to ensure percolation of the electrolyte to the electrodes. The discharge and charge measurements were carried out on an Arbin battery test system (BT2000) in the voltage window of 0.01–3.0 V at various current densities. The cycling voltammogram (CV) test also was performed on a multichannel battery tester (model SCN, USA) at a scan rate of 0.05 mV s^{-1}.

Supporting Information

Supporting Information is available from the Wiley Online Library or from the author.

Acknowledgements

This work was financially supported by 973 Program (Grant No. 2013CB632701), the National Natural Science Foundation of China (Grant No. 51202163), Shanghai Pujiang Program (Grant No. 12PJ1408200), the Innovation Program of Shanghai Municipal Education Commission (Grant No. 13ZZ025), Doctor Programs Foundation of MOE (20120072120044) and the Fundamental Research Fund for Central University.

Received: December 18, 2013
Revised: January 19, 2014
Published online: March 14, 2014

[1] J. M. Tarascon, M. Armand, *Nature* **2001**, *414*, 359.
[2] X. W. Lou, L. A. Archer, Z. C. Yang, *Adv. Mater.* **2008**, *20*, 3987.
[3] C. Guan, J. P. Liu, C. W. Cheng, H. X. Li, X. L. Li, W. W. Zhou, H. Zhang, H. J. Fan, *Energy Environ. Sci.* **2011**, *4*, 4496.
[4] B. G. Choi, M. H. Yang, W. H. Hong, J. W. Choi, Y. S. Huh, *ACS Nano* **2012**, *6*, 4020.
[5] Y. J. Chen, B. H. Qu, L. L. Hu, Z. Xu, Q. H. Li, T. H. Wang, *Nanoscale* **2013**, *5*, 9812.
[6] Y. G. Zhu, Y. Wang, Y. M. Shi, J. I. Wong, H. Y. Yang, *Nano Energy* **2014**, *3*, 46.
[7] P. Simon, Y. Gogotsi, *Nat. Mater.* **2008**, *7*, 845.
[8] A. Manthiram, J. Kim, *Chem. Mater.* **1998**, *10*, 2895.
[9] M. G. Kim, J. Cho, *Adv. Funct. Mater.* **2009**, *19*, 1497.
[10] M. Armand, J. M. Tarascon, *Nature* **2008**, *451*, 652–657.
[11] P. G. Bruce, B. Scrosat, J. M. Tarascon, *Angew. Chem., Int. Ed.* **2008**, *47*, 2930.
[12] J. B. Goodenough, Y. Kim, *Chem. Mater.* **2010**, *22*, 587.
[13] C. H. Xu, B. H. Xu, Y. Gu, Z. G. Xiong, J. Sun, X. S. Zhao, *Energy Environ. Sci.* **2013**, *6*, 1388.
[14] Z. Y. Guo, J. Wang, F. Wang, D. D. Zhou, Y. Y. Xia, Y. G. Wang, *Adv. Funct. Mater.* **2013**, *23*, 4759.
[15] S. Boukhalfa, K. Evanoff, G. Yushin, *Energy Environ. Sci.* **2012**, *5*, 6872.
[16] X. H. Xia, J. P. Tu, Y. Q. Zhang, X. L. Wang, C. D. Gu, X. B. Zhao, H. J. Fan, *ACS Nano* **2012**, *6*, 5531.
[17] H. Wu, M. Xu, H. Y. Wu, J. J. Xu, Y. L. Wang, Z. Peng, G. F. Zheng, *J. Mater. Chem.* **2012**, *22*, 19821.
[18] C. W. Cheng, H. J. Fan, *Nano Today* **2012**, *7*, 327.
[19] L. Nyholm, G. Nyström, A. Mihranyan, M. Strømme, *Adv. Mater.* **2011**, *23*, 3751.
[20] G. Nyström, A. Razaq, M. Strømme, L. Nyholm, A. Mihranyan, *Nano Lett.* **2009**, *9*, 3635.
[21] D. P. Dubal, S. H. Lee, J. G. Kim, W. B. Kim, C. D. Lokhande, *J. Mater. Chem.* **2012**, *22*, 3044.
[22] Y. S. Luo, J. S. Luo, J. Jiang, W. W. Zhou, H. P. Yang, X. Y. Qi, H. Zhang, H. J. Fan, D. Y. W. Yu, C. M. Li, T. Yu, *Energy Environ. Sci.* **2012**, *5*, 6559.
[23] W. W. Zhou, C. W. Cheng, J. P. Liu, Y. Y. Tay, J. Jiang, X. T. Jia, J. X. Zhang, H. Gong, H. H. Hng, T. Yu, H. J. Fan, *Adv. Func. Mater.* **2011**, *21*, 2439.
[24] J. S. Luo, X. H. Xia, Y. S. Luo, C. Guan, J. L. Liu, X. Y. Qi, C. F. Ng, T. Yu, H. Zhang, H. J. Fan, *Adv. Energy Mater.* **2013**, *3*, 737.
[25] H. N. Zhang, Y. J. Chen, W. W. Wang, G. H. Zhang, M. Zhuo, H. M. Zhang, T. Yang, Q. H. Li, T. H. Wang, *J. Mater. Chem. A* **2013**, *1*, 8593.

[26] G. Yu, L. Hu, M. Vosgueritchian, H. Wang, X. Xie, J. R. McDonough, X. Cui, Y. Cui, Z. Bao, *Nano Lett.* **2011**, *11*, 2905.
[27] Z. Li, Y. Mi, X. Liu, S. Liu, S. Yang, J. J. Wang, *Mater. Chem.* **2011**, *21*, 14706.
[28] W. Wei, X. Cui, W. Chen, D. G. Ivey, *Chem. Soc. Rev.* **2011**, *40*, **1697**.
[29] L. Wei, C. Li, H. Chu, Y. Li, *Dalton Trans.* **2011**, *40*, 2332.
[30] M. J. Deng, J. K. Chang, C. C. Wang, K. W. Chen, C. M. Lin, M. T. Tang, J. M. Chen, K. T. Lu, *Energy Environ. Sci.* **2011**, *4*, 3942.
[31] Y. Hou, Y. Cheng, T. Hobson, J. Liu, *Nano Lett.* **2010**, *10*, 2727.
[32] C. Meng, C. Liu, L. Chen, C. Hu, S. Fan, *Nano Lett.* **2010**, *10*, 4025.
[33] S. W. Lee, J. Kim, S. Chen, P. T. Hammond, Y. Shao-Horn, *ACS Nano* **2010**, *4*, 3889.
[34] J. Liu, J. Essner, J. Li, *Chem. Mater.* **2010**, *22*, 5022.
[35] Y. M. He, W. J. Chen, X. D. Li, Z. X. Zhang, J. C. Fu, C. H. Zhao, E. Q. Xie, *ACS Nano* **2013**, *7*, 174.
[36] A. P. Yu, H. W. Park, A. Davies, D. C. Higgins, Z. W. Chen, X. C. Xiao, *J. Phys. Chem. Lett.* **2011**, *2*, 1855.
[37] J. P. Liu, J. Jiang, C. W. Cheng, H. X. Li, J. X. Zhang, H. Gong, H. J. Fan, *Adv. Mater.* **2011**, *23*, 2076.
[38] W. Y. Li, G. Li, J. Q. Sun, R. J. Zou, K. B. Xu, Y. G. Sun, Z. G. Chen, J. M. Yang, J. Q. Hu, *Nanoscale* **2013**, *5*, 2901.
[39] Y. Wang, F. Yan, S. W. Liu, A. Y. S. Tan, H. Song, X. W. Sun, H. Y. Yang, *J. Mater. Chem. A* **2013**, *1*, 5212.
[40] Y. S. Luo, D. Z. Kong, J. S. Luo, S. Chen, D. Y. Zhang, K. W. Qiu, X. Y. Qi, H. Zhang, C. M. Li, Ting Yu, *RSC Adv.* **2013**, *3*, 14413.
[41] J. Jiang, L. C. Li, *Mater. Lett.* **2007**, *61*, 4894.
[42] H. Jiang, C. Z. Li, T. Sun, J. Ma, *Chem. Commun.* **2012**, *48*, 2606.
[43] A. L. M. Reddy, M. M. Shaijumon, S. R. Gowda, P. M. Ajayan, *Nano Lett.* **2009**, *9*, 1002.
[44] W. Y. Li, L. N. Xu, J. Chen, *Adv. Funct. Mater.* **2005**, *15*, 851.
[45] X. H. Wang, X. W. Li, X. L. Sun, F. Li, Q. M. Liu, Q. Wang, D. Y. He, *J. Mater. Chem.* **2011**, *21*, 3571.
[46] X. Zhu, Y. Zhu, S. Murali, M. D. Stoller, R. S. Ruoff, *ACS Nano* **2011**, *5*, 3333.